Computers and Fluids 179 (2019) 277–288

Contents lists available at ScienceDirect

Computers and Fluids

journal homepage: www.elsevier.com/locate/compfluid

Analysis and assessment of a monolithic FSI finite element method☆

Alexander Lozovskiy[a], Maxim A. Olshanskii[b,*], Yuri V. Vassilevski[c]

[a] Marchuk Institute of Numerical Mathematics RAS, Russia
[b] Department of Mathematics, University of Houston, USA
[c] Marchuk Institute of Numerical Mathematics RAS, Moscow Institute of Physics and Technology, Lomonosov Moscow State University, Sechenov University, Russia

ARTICLE INFO

Article history:
Received 25 April 2018
Revised 9 October 2018
Accepted 5 November 2018
Available online 6 November 2018

ABSTRACT

In this paper we analyze and investigate numerically a monolithic finite element method for the incompressible Navier–Stokes equations coupled to the Saint Venant–Kirchhoff hyperelastic model. The approach strongly enforces the coupling conditions on the fluid–structure interface and treats both solid and fluid equations in a reference domain accounting for geometric motion through time-dependent coefficients. The paper derives an energy balance for the fully discrete system and proves that the finite element method is numerically stable. The performance of the method is further assessed by validating numerical results for the pressure impulse prorogation test and against the results of a recently proposed experimental 3D fluid-structure interaction benchmark problem.

1. Introduction

Many practically interesting problems of fluid dynamics involve mutual interaction of a fluid and an elastic structure: Fluid flow depends on the structure displacement, while structure motion is influenced by the fluid dynamics. In mathematical modeling such setup is known as a fluid–structure interaction (FSI) problem. Examples of FSI problems arise in structural and fluid mechanics, aerodynamics, and cardiovascular system modeling [8,16,20]. Numerical simulation plays an increasingly important role in understanding and prediction of fluid–structure interaction phenomena in many engineering and life science applications [6,29,51].

A typical FSI model includes equations governing the fluid dynamics and the motion of elastic materials together with coupling conditions at the fluid–structure interface. The Navier-Stokes equations of fluid dynamics are nonlinear parabolic and are commonly given in the Eulerian coordinates, while for solids motion one usually considers Lagrangian description, which results in a hyperbolic equation for the displacement variable. Thus, an FSI problem poses the numerical challenge of handling a coupled system of nonlinear equations of mixed type given in Eulerian and Lagrangian frames of references.

The numerical method studied in this paper falls into the category of monolithic approaches [22,29–31,40,42,45,53] that treat the fluid and the structure as a single continuum. In a monolithic approach, the coupling conditions at interface are implicit to the solution procedure. This is opposite to the alternative partitioned approach [3,12,13,35,41,44,52], when the fluid and the structure are treated separately, and one consequently solves fluid and structure subproblems in the course of simulation. In general, monolithic methods are known to be more robust and stable, especially for unsteady FSI problems. This robustness comes with the expense of more computationally demanding algebraic systems to be solved; see, e.g. [25] for comparison. One of the popular approaches to deal with the discrepancy between Eulerian and Lagrangian formulations for fluid and solid is the Arbitrary Lagrangian-Eulerian (ALE) method [15,28,32]. In the scope of ALE method, the structure is presented in Lagrangian coordinates whereas the fluid flow is considered in an artificial coordinate system. This system is given by an auxiliary mapping from the reference fluid domain to the physical one. Further, in the ALE method one handles the time derivative in the reference domain, but often treats all other terms of the fluid equations in the physical domain. We note that ALE formulation is not the only possible choice for a monolithic approach. One may adopt a pure Eulerian description of the fluid and structure motion [17] or treat both in a fully Lagrangian way [45]. Among the most recent studies of monolithic FSI methods we mention [4], which applies the ALE description for the fluid but allows for large displacements of 1D coupled structures, [46] and [55], where monolithic methods with fully Lagrangian description of fluid and structure motion were applied for incompressible

☆ This work has been supported by the Russian Science Foundation (RSF) grant 14-31-00024.

* Corresponding author.
E-mail addresses: saiya-jin@yandex.ru (A. Lozovskiy), molshan@math.uh.edu (M.A. Olshanskii), yuri.vassilevski@gmail.com (Y.V. Vassilevski).

https://doi.org/10.1016/j.compfluid.2018.11.004
0045-7930/

and quasi-compressible fluids, respectively, and [2] that focused on building an efficient algebraic solver for ALE/Lagrangian formulation for incompressible fluids and elasticity.

To solve the FSI problem, we use an ALE formulation for the discretization of equations in the reference time-independent domain. The geometry evolution is accounted for by the time-dependent coefficients. For this formulation, the paper introduces a finite element method. Thus we effectively have a method of lines for the coupled system with a finite difference approach to handle time dependence. Other options available in the literature include space–time finite element monolithic [31,49] or hybrid [40] formulations. We carry out full stability analysis for the case of the implicit Euler time discretization. We note that numerical analysis of a finite element method for the FSI problem is challenging due to the non-linearity of the system and its mixed hyperbolic–parabolic type. Several stability analyses are known from the literature often in simplified settings; see, e.g., [9,19,24,37,43,47,54]. In the present paper, we show the correct energy balance and prove the unconditional (without a time-step restriction) stability of a fully discrete method. We note that no full error analysis is known for FSI problems, the full error analysis of the quasi-Lagrangian (mesh nodes do not follow fluid particles) FE method for fluid equations in a time-dependent domain (no elasticity model is included) became available in [38] only recently.

The FSI FE method is further validated numerically on a set of two benchmark problems. The first one is the well-known pressure wave propagation in an elastic cylindrical tube filled with viscous incompressible fluid [21]. The second one is the recently introduced challenging benchmark test [26] that involves steady and periodic interactions between a viscous incompressible fluid and a nonlinear solid filament in a 3D setting. For this test, numerical results are assessed against experimental data collected using phase-contrast magnetic resonance imaging.

The outline of the remainder of the paper is the following. Section 2 introduces governing equations, suitable interface and boundary conditions and recalls the fundamental energy balance equality satisfied by all smooth solutions to the system. In Section 3 we present the discretization method. The method is analyzed in Section 4, where suitable *a priori* energy estimates for numerical solutions are shown. Section 5 collects the results of numerical experiments and compares them to available experimental data. The method is implemented using the open source package Ani3D [36].

2. Problem formulation

Consider a time-dependent domain $\Omega(t) \subset \mathbb{R}^3$, partitioned into subdomains $\Omega^f(t)$ and $\Omega^s(t)$ occupied by fluid and solid, respectively. Let $\Gamma^{fs}(t) := \partial\Omega^f(t) \cap \partial\Omega^s(t)$ be the interface where the interaction of the fluid and solid takes place. Denote the reference domains by

$$\Omega_f = \Omega^f(0), \quad \Omega_s = \Omega^s(0), \quad \Gamma_{fs} = \Gamma^{fs}(0),$$

and the deformation of the solid medium by

$$\boldsymbol{\xi}^s \ : \ \Omega_s \times [0,t] \to \bigcup_{t\in[0,T]} \Omega^s(t),$$

with the corresponding displacement $\mathbf{u}^s$ given by $\mathbf{u}^s(\mathbf{x},t) := \boldsymbol{\xi}^s(\mathbf{x},t) - \mathbf{x}$ and velocity $\mathbf{v}^s := \partial_t \mathbf{u}^s = \partial_t \boldsymbol{\xi}^s(\mathbf{x},t)$.

For the fluid, we adopt an ALE formulation by introducing an auxiliary mapping

$$\boldsymbol{\xi}^f \ : \ \Omega_f \times [0,t] \to \bigcup_{t\in[0,T]} \Omega^f(t)$$

such that $\boldsymbol{\xi}^s = \boldsymbol{\xi}^f$ on Γ_{fs}. The mapping is defined by a continuous extension of the displacement field $\mathbf{u}^s$ to the flow reference domain

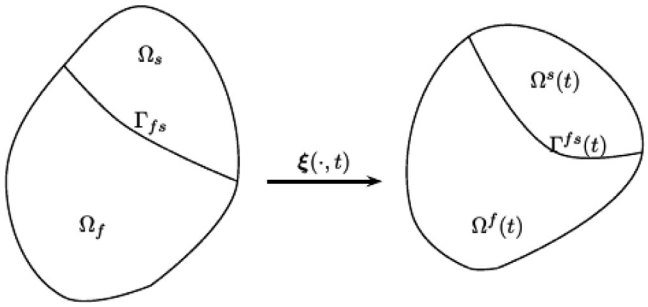

Fig. 1. Mapping of the reference solid and fluid domains to the currrent configuration.

$$\mathbf{u}^f := \mathrm{Ext}(\mathbf{u}^s) = \boldsymbol{\xi}^f(\mathbf{x},t) - \mathbf{x} \quad \text{in } \Omega_f \times [0,t]. \tag{1}$$

The extension $\mathrm{Ext}(\mathbf{u}^s)$ can be provided by a PDE solution in $\Omega_f \times [0, t]$. Mapping $\boldsymbol{\xi}^f$ is not Lagrangian since it does not follow fluid particles trajectories. Fig. 1 illustrates the mapping.

The fluid dynamics is described by the velocity vector field $\mathbf{v}^f$ and the pressure scalar field p^f defined in current domain $\Omega^f(t)$ for $t \in [0, T]$. From now on, for notational simplicity, we will be using the same notation for these fields redefined on the reference configuration as $\mathbf{v}^f(\mathbf{x}, t) := \mathbf{v}^f(\boldsymbol{\xi}^f(\mathbf{x}, t), t)$ and $p^f(\mathbf{x}, t) := p^f(\boldsymbol{\xi}^f(\mathbf{x}, t), t)$.

Following [30] we consider a monolithic numerical approach using the continuous globally defined displacement and velocity fields

$$\mathbf{u} = \begin{cases} \mathbf{u}^s & \text{in } \Omega_s, \\ \mathbf{u}^f & \text{in } \Omega_f, \end{cases} \qquad \mathbf{v} = \begin{cases} \mathbf{v}^s & \text{in } \Omega_s, \\ \mathbf{v}^f & \text{in } \Omega_f. \end{cases}$$

The corresponding globally defined deformation gradient is $\mathbf{F} = \mathbf{I} + \nabla\mathbf{u}$. Its determinant will be denoted by $J := \det(\mathbf{F})$.

Denote by ρ_s and $\rho_f = \text{const}$ the densities of solid and fluid, and by $\boldsymbol{\sigma}_s$, $\boldsymbol{\sigma}_f$ the Cauchy stress tensors, so that $J(\boldsymbol{\sigma}_s \circ \boldsymbol{\xi}^s)\mathbf{F}^{-T}$ is the Piola-Kirchhoff tensor in the structure, with $\boldsymbol{\sigma}_s \circ \boldsymbol{\xi}^s(\mathbf{x}) := \boldsymbol{\sigma}_s(\boldsymbol{\xi}^s(\mathbf{x}))$.

The conservation of momentum equations for the solid and fluid written in the Lagrangian and ALE coordinates, respectively, takes the form

$$\frac{\partial \mathbf{v}}{\partial t} = \begin{cases} \rho_s^{-1}\mathrm{div}(J(\boldsymbol{\sigma}_s \circ \boldsymbol{\xi}^s)\mathbf{F}^{-T}) & \text{in } \Omega_s, \\ (J\rho_f)^{-1}\mathrm{div}(J(\boldsymbol{\sigma}_f \circ \boldsymbol{\xi}^f)\mathbf{F}^{-T}) - (\nabla\mathbf{v})\left(\mathbf{F}^{-1}\left(\mathbf{v} - \dfrac{\partial \mathbf{u}}{\partial t}\right)\right) & \text{in } \Omega_f. \end{cases} \tag{2}$$

The definition of $\mathbf{v}$ in the solid domain gives

$$\frac{\partial \mathbf{u}}{\partial t} = \mathbf{v} \quad \text{in } \Omega_s. \tag{3}$$

For incompressible fluid, the conservation of mass equation in the reference domain reads:

$$\mathrm{div}(J\mathbf{F}^{-1}\mathbf{v}) = 0 \quad \text{in } \Omega_f. \tag{4}$$

On the fluid–structure interface, we assume no-slip no-penetration of fluid and the balance of normal stresses,

$$\mathbf{v}^s = \mathbf{v}^f \quad \text{and} \quad \boldsymbol{\sigma}_f\mathbf{F}^{-T}\mathbf{n} = \boldsymbol{\sigma}_s\mathbf{F}^{-T}\mathbf{n} \quad \text{on } \Gamma_{fs}, \tag{5}$$

where $\mathbf{n}$ is the unit normal vector on Γ_{fs}.

To prescribe boundary conditions on $\partial\Omega(0)$, we distinguish between the structure boundary $\Gamma_{s0} := \partial\Omega(0) \cap \partial\Omega_s$, fluid Dirichlet and outflow boundaries: $\partial\Omega(0) \cap \partial\Omega_f = \Gamma_{f0} \cup \Gamma_{\text{out}}$. Depending on the type of the boundary, the following conditions are imposed:

$$\begin{aligned} &\mathbf{v} = \mathbf{g}_D \ \text{ on } \Gamma_{f0}, \quad \boldsymbol{\sigma}_f\mathbf{F}^{-T}\mathbf{n} = \mathbf{g}_N + \tfrac{\rho_f\kappa}{2}(\mathbf{v}\cdot\mathbf{n})_-\mathbf{v} \ \text{ on } \Gamma_{\text{out}}, \\ &\mathbf{u} = \mathbf{0} \ \text{ on } \Gamma_{s0} \cup \Gamma_{f0} \cup \Gamma_{\text{out}}, \end{aligned} \tag{6}$$

where $(f)_\pm := \frac{1}{2}(f \pm |f|)$, $\mathbf{n}$ is the outward unit normal vector on Γ_{out}, and $\kappa \in [0, 1]$ is a parameter introduced to stabilize the

system against nonphysical energy increase produced by backflow phenomenon on Γ_{out}; see, e.g., [7]. Stabilized outflow conditions are found in many places in the literature, e.g. [5]. For $\kappa = 1$, they were analyzed as "directional do-nothing condition" in [10]. Their stabilizing effect will become clear from the energy balance (12), where κ close to 1 is seen to ensure decay of the numerical energy. The governing equations are complemented with initial conditions

$$\mathbf{u}(\mathbf{x}, 0) = \mathbf{0}, \quad \mathbf{v}(\mathbf{x}, 0) = \mathbf{v}_0(\mathbf{x}) \ \text{ on } \Omega(0). \tag{7}$$

We assume the fluid to be Newtonian, with the viscosity parameter μ_f. In the ALE coordinates, the Cauchy tensor of Newtonian fluid is given by

$$\boldsymbol{\sigma}_f = -p_f \mathbf{I} + \mu_f (\nabla \mathbf{v} \mathbf{F}^{-1} + \mathbf{F}^{-T} (\nabla \mathbf{v})^T) \quad \text{in } \Omega_f. \tag{8}$$

For the structure we consider the compressible geometrically nonlinear Saint Venant–Kirchhoff material with

$$\boldsymbol{\sigma}_s = \frac{1}{J} \mathbf{F} (\lambda_s \text{tr}(\mathbf{E}) \mathbf{I} + 2\mu_s \mathbf{E}) \mathbf{F}^T, \tag{9}$$

where $\mathbf{E} = \frac{1}{2}\left(\mathbf{F}^T\mathbf{F} - \mathbf{I}\right)$ is the Lagrange-Green strain tensor and λ_s, μ_s are the Lame constants. Both analysis and numerical experiments in this paper are restricted to the Saint Venant–Kirchhoff material since material parameters in 3D benchmark problems addressed in Section 5 are given for this material. The method, however, can be easily extended to neo-Hookean materials [37].

For the notation convenience, we set $p_s = 0$ in Ω_s and define the global pressure variable by

$$p = \begin{cases} p_f & \text{in } \Omega_f, \\ p_s & \text{in } \Omega_s. \end{cases}$$

Thus, the FSI problem consists in finding pressure distribution p and continuous velocity and displacement fields **v, u** satisfying the set of equations, interface and boundary conditions (2)–(9) and subject to a provided extension rule (1).

We note a few identities that are useful for the design of a numerical method and its analysis. In the fluid region the mass balance yields the equation

$$\frac{\partial J}{\partial t} + \text{div}\left(J \mathbf{F}^{-1} \left(\mathbf{v} - \frac{\partial \mathbf{u}}{\partial t} \right) \right) = 0 \quad \text{in } \Omega_f. \tag{10}$$

Furthermore, the Piola identity $\text{div}(J\mathbf{F}^{-1}) = 0$ implies the following equality

$$\text{div}(J\mathbf{F}^{-1}\mathbf{v}) = J(\nabla \mathbf{v}) : \mathbf{F}^{-T} \quad \text{in } \Omega_f, \tag{11}$$

where $\mathbf{A} : \mathbf{B} := \sum_{i,j=1}^{N} A_{ij} B_{ij}$.

For homogeneous boundary conditions, one shows with the help of (10)–(11) that any smooth solution to (2)–(9) satisfies the energy equality, cf. [37],

$$\begin{aligned} &\frac{1}{2}\frac{d}{dt}\left(\int_{\Omega_s} \rho_s \left| \frac{\partial \mathbf{u}}{\partial t} \right|^2 \mathrm{d}\mathbf{x} + \rho_f \int_{\Omega_f} J|\mathbf{v}|^2 \,\mathrm{d}\mathbf{x} + \int_{\Omega_s} (\lambda_s \text{tr}(\mathbf{E})^2 + 2\mu_s |\mathbf{E}|_F^2) \,\mathrm{d}\mathbf{x} \right) \\ &+ 2\mu_f \int_{\Omega_f} J |\mathbf{D}_{\mathbf{u}}(\mathbf{v})|_F^2 \,\mathrm{d}\mathbf{x} + \frac{\rho_f}{2} \int_{\Gamma_{\text{out}}} \{ (\mathbf{v}\cdot\mathbf{n})_+ \\ &+ (1-\kappa)(\mathbf{v}\cdot\mathbf{n})_- \} |\mathbf{v}|^2 \,\mathrm{d}\mathbf{s} = 0, \end{aligned} \tag{12}$$

where $\mathbf{D}_{\mathbf{u}}\mathbf{v} := \frac{1}{2}\left((\nabla \mathbf{v})\mathbf{F}^{-1}(\mathbf{u}) + \mathbf{F}^{-T}(\mathbf{u})(\nabla \mathbf{v})^T \right)$ and $|\ldots|_F$ denotes the matrix Frobenius norm. In the energy equality (12) the variation of the total system energy is balanced by the fluid viscous dissipation and the energy rate at the open boundary. Note that for $\kappa = 1$ the last term is non-negative.

3. Discretization

In this section we introduce both time and space discretization of the FSI problem. Treating the problem in the reference domain allows us to avoid triangulations and finite element function spaces dependent on time. For an alternative approach based on space-time finite element methods see, for example, [49,50]. We consider a collection of tetrahedra, which form a consistent regular tessellation of the reference domain $\overline{\Omega}(0) = \overline{\Omega}_s \cup \overline{\Omega}_f$. In the monolithic approach we consider conforming FE spaces $\mathbb{V}_h \subset H^1(\Omega(0))^3$ and $\mathbb{Q}_h \subset L^2(\Omega(0))$ for trial functions and the following two subspaces for the test functions: $\mathbb{V}_h^0 = \{\mathbf{v} \in \mathbb{V}_h : \mathbf{v}|_{\Gamma_{s0} \cup \Gamma_{f0}} = \mathbf{0}\}$ and $\mathbb{V}_h^{00} = \{\mathbf{v} \in \mathbb{V}_h^0 : \mathbf{v}|_{\Gamma_{sf}} = \mathbf{0}\}$. We assume that $\mathbb{V}_h^0$ and $\mathbb{Q}_h$ form the LBB-stable finite element pair: There exists a mesh-independent constant c_0, such that

$$\inf_{q_h \in \mathbb{Q}_h} \sup_{\mathbf{v}_h \in \mathbb{V}_h^0} \frac{(q_h, \text{div}\mathbf{v}_h)}{\|\nabla \mathbf{v}_h\| \|q_h\|} \geq c_0 > 0.$$

Assuming a constant time step Δt, we use the notation $\mathbf{u}^k(\mathbf{x}) \approx \mathbf{u}(k\Delta t, \mathbf{x})$. The backward finite difference approximation of the time derivative at $t = k\Delta t$ is denoted by

$$\left[\frac{\partial \mathbf{u}}{\partial t} \right]^k = \frac{\mathbf{u}^k - \mathbf{u}^{k-1}}{\Delta t}.$$

Similar notation is used for $\mathbf{v}$, p and other time-dependent quantities.

To formulate the discretization method, we need some further notations. For $\mathbf{F}(\mathbf{u}) = \mathbf{I} + \nabla \mathbf{u}$, $\mathbf{E}(\mathbf{u}) = \frac{1}{2}\left(\mathbf{F}(\mathbf{u})^T \mathbf{F}(\mathbf{u}) - \mathbf{I} \right)$ we define $\mathbf{S}(\mathbf{u}) = \lambda_s \text{tr}(\mathbf{E}(\mathbf{u}))\mathbf{I} + 2\mu_s \mathbf{E}(\mathbf{u})$, $\mathbf{F}_k = \mathbf{F}(\mathbf{u}^k)$, $J_k = \det(\mathbf{F}_k)$, $\mathbf{E}_k = \mathbf{E}(\mathbf{u}^k)$, $\mathbf{S}_k = \mathbf{S}(\mathbf{u}^k)$, $\mathbf{D}_k = \mathbf{D}_{\mathbf{u}^k}$, and $\mathbf{F}_{k+\frac{1}{2}} = \frac{1}{2}(\mathbf{F}_k + \mathbf{F}_{k+1})$.

The finite element method for the ALE monolithic FSI formulation reads: Given $\{\mathbf{u}^{k-1}, \mathbf{v}^{k-1}\} \in \mathbb{V}_h^0 \times \mathbb{V}_h$ find $\{\mathbf{u}^k, \mathbf{v}^k, p^k\} \in \mathbb{V}_h^0 \times \mathbb{V}_h \times \mathbb{Q}_h$ such that $\mathbf{v}^k = \mathbf{g}_D(\cdot, k\Delta t)$ on Γ_{f0} and the following equations hold:

$$\begin{aligned} &\int_{\Omega_s} \rho_s \left[\frac{\partial \mathbf{v}}{\partial t} \right]^k \boldsymbol{\psi} \,\mathrm{d}\mathbf{x} + \int_{\Omega_s} \mathbf{F}_{k-\frac{1}{2}} \mathbf{S}_k : \nabla \boldsymbol{\psi} \,\mathrm{d}\mathbf{x} \\ &+ \int_{\Omega_f} \rho_f J_{k-1} \left[\frac{\partial \mathbf{v}}{\partial t} \right]^k \boldsymbol{\psi} \,\mathrm{d}\mathbf{x} + \int_{\Omega_f} \rho_f J_k (\nabla \mathbf{v}^k) \mathbf{F}_k^{-1} \left(\mathbf{v}^k - \left[\frac{\partial \mathbf{u}}{\partial t} \right]^k \right) \boldsymbol{\psi} \,\mathrm{d}\mathbf{x} \\ &+ \int_{\Omega_f} 2\mu_f J_k \mathbf{D}_k \mathbf{v}^k : \mathbf{D}_k \boldsymbol{\psi} \,\mathrm{d}\mathbf{x} - \int_{\Omega_f} p^k J_k \mathbf{F}_k^{-T} : \nabla \boldsymbol{\psi} \,\mathrm{d}\mathbf{x} \\ &+ \int_{\Omega_f} \frac{\rho_f}{2} \left(\left[\frac{\partial J}{\partial t} \right]^k + \text{div}\left(J_k \mathbf{F}_k^{-1} \left(\mathbf{v}^k - \left[\frac{\partial \mathbf{u}}{\partial t} \right]^k \right) \right) \right) \boldsymbol{\psi} \,\mathrm{d}\mathbf{x} \\ &\quad = \int_{\Gamma_{\text{out}}} (\mathbf{g}_N + \frac{\rho_f \kappa}{2} (\mathbf{v}^k \cdot \mathbf{n})_- \mathbf{v}^k) \cdot \boldsymbol{\psi} \,\mathrm{d}\mathbf{s} \end{aligned} \tag{13}$$

for all $\boldsymbol{\psi} \in \mathbb{V}_h^0$,

$$\int_{\Omega_s} \left[\frac{\partial \mathbf{u}}{\partial t} \right]^k \boldsymbol{\phi} \,\mathrm{d}\mathbf{x} - \int_{\Omega_s} \mathbf{v}^k \boldsymbol{\phi} \,\mathrm{d}\mathbf{x} = 0 \tag{14}$$

for all $\boldsymbol{\phi} \in \mathbb{V}_h^{00}$, and

$$\int_{\Omega_f} J_k (\nabla \mathbf{v}^k) : \mathbf{F}_k^{-T} q \,\mathrm{d}\mathbf{x} = 0 \tag{15}$$

for all $q \in \mathbb{Q}_h$. The integrals over the interface in (13) cancel out due to the interface condition (5). The coupling condition on Γ_{sf} is enforced strongly,

$$\left[\frac{\partial \mathbf{u}}{\partial t} \right]^k = \mathbf{v}^k \quad \text{on } \Gamma_{sf}. \tag{16}$$

In other words, for all degrees of freedom corresponding to the interface nodes, we add equations $\frac{1}{\Delta t}\mathbf{u}_k - \mathbf{v}_k = \frac{1}{\Delta t}\mathbf{u}_{k-1}$ to the total algebraic system for the unknowns $\mathbf{u}_k$ and $\mathbf{v}_k$. Hence, (16) is satisfied up to the accuracy of our algebraic solver. This together with (14) implies the equality $\left[\frac{\partial \mathbf{u}}{\partial t}\right]^k = \mathbf{v}^k$ is satisfied pointwise in Ω_s.

Eqs. (13)–(16) subject to initial conditions and a choice of continuous extension of $\mathbf{u}^k$ from Ω_s onto Ω_f ensuring $\mathbf{u}^k \in \mathbb{V}_h^0$ define the discrete problem. We shall use an extension based on auxiliary elasticity equation, see Section 5.

Remark 1. The last term in the left-hand side of (13) is consistent due to the identity (10) and is added in the FE formulation to enforce the conservation property of the discretization. While computations show that in practice this term can be skipped, stability analysis benefits from including it. In the analysis of FEM for incompressible Navier-Stokes equations in the Eulerian description, including this term corresponds to the Temam's [48] skew-symmetric form of the convective terms.

4. Numerical stability

In this section, we show energy balance and stability estimate for the solution to (13)–(16). As common in the stability analysis, we consider the homogeneous boundary conditions on Γ_{f0}, i.e. $\mathbf{g}_D = \mathbf{0}$ in (6).

Note the following identities:

$$\begin{aligned} 2\mathbf{F}^T_{k-\frac12}(\nabla\mathbf{u}^k - \nabla\mathbf{u}^{k-1}) &= 2\mathbf{F}^T_{k-\frac12}(\mathbf{F}_k - \mathbf{F}_{k-1}) \\ &= \mathbf{F}_k^T\mathbf{F}_k - \mathbf{F}_{k-1}^T\mathbf{F}_{k-1} + \left(\mathbf{F}_{k-1}^T\mathbf{F}_k - \mathbf{F}_k^T\mathbf{F}_{k-1}\right) \\ &= 2(\mathbf{E}_k - \mathbf{E}_{k-1}) + \mathcal{N}, \end{aligned} \tag{17}$$

where $\mathcal{N}$ is skew-symmetric. For arbitrary real square matrices A, B, C, it follows from the definition of trace that $AB : C = \mathrm{tr}(ABC^T) = \mathrm{tr}(BC^TA) = B : A^TC$. Thus, it holds

$$\mathbf{F}_{k-\frac12}\mathbf{S}_k : (\nabla\mathbf{u}^k - \nabla\mathbf{u}^{k-1}) = \mathbf{S}_k : \mathbf{F}^T_{k-\frac12}(\nabla\mathbf{u}^k - \nabla\mathbf{u}^{k-1}).$$

Due to the symmetry of $\mathbf{S}_k$ it holds $\mathbf{S}_k : \mathcal{N} = 0$ and we get from (17)

$$\mathbf{F}_{k-\frac12}\mathbf{S}_k : (\nabla\mathbf{u}^k - \nabla\mathbf{u}^{k-1}) = \mathbf{S}_k : (\mathbf{E}_k - \mathbf{E}_{k-1}). \tag{18}$$

Now we set in (13)

$$\boldsymbol{\psi} = \begin{cases} \left[\frac{\partial \mathbf{u}}{\partial t}\right]^k & \text{in } \Omega_s, \\ \mathbf{v}^k & \text{in } \Omega_f. \end{cases}$$

Thanks to (16), $\boldsymbol{\psi}$ is a suitable test function, i.e. $\boldsymbol{\psi} \in \mathbb{V}_h^0$. We handle each resulting term separately and start with the first term in (13):

$$\begin{aligned} \int_{\Omega_s} \rho_s \left[\frac{\partial \mathbf{v}}{\partial t}\right]^k \boldsymbol{\psi}\,\mathrm{d}\mathbf{x} &= \int_{\Omega_s} \rho_s \left(\frac{\mathbf{v}^k - \mathbf{v}^{k-1}}{\Delta t}\right)\left(\frac{\mathbf{u}^k - \mathbf{u}^{k-1}}{\Delta t}\right)\mathrm{d}\mathbf{x} \\ &= \int_{\Omega_s} \rho_s \left(\frac{\mathbf{v}^k - \mathbf{v}^{k-1}}{\Delta t}\right)\mathbf{v}^k\,\mathrm{d}\mathbf{x} \\ &= \frac{1}{2\Delta t}\left(\|\rho_s^{\frac12}\mathbf{v}^k\|^2_{\Omega_s} - \|\rho_s^{\frac12}\mathbf{v}^{k-1}\|^2_{\Omega_s}\right) \\ &\quad + \frac{|\Delta t|}{2}\left\|\rho_s^{\frac12}\left[\frac{\partial \mathbf{v}}{\partial t}\right]^k\right\|^2_{\Omega_s}. \end{aligned} \tag{19}$$

Here and further $\|\cdot\|_{\Omega_s}$ denotes the $L^2(\Omega_s)$ norm. Thanks to (17) and (18) we obtain for the second term in (13):

$$\begin{aligned} \int_{\Omega_s} \mathbf{F}_{k-\frac12}\mathbf{S}_k : \nabla\boldsymbol{\psi}\,\mathrm{d}\mathbf{x} &= \frac{1}{\Delta t}\int_{\Omega_s} \mathbf{S}_k : (\mathbf{E}_k - \mathbf{E}_{k-1})\,\mathrm{d}\mathbf{x} \\ &= \frac{\lambda_s}{2\Delta t}\left(\|\mathrm{tr}(\mathbf{E}_k)\|^2_{\Omega_s} - \|\mathrm{tr}(\mathbf{E}_{k-1})\|^2_{\Omega_s}\right) \\ &\quad + \frac{\mu_s}{\Delta t}\left(\|\mathbf{E}_k\|^2_{\Omega_s} - \|\mathbf{E}_{k-1}\|^2_{\Omega_s}\right) \\ &\quad + \frac{\lambda_s\Delta t}{2}\left\|\left[\frac{\partial \mathrm{tr}(\mathbf{E})}{\partial t}\right]^k\right\|^2_{\Omega_s} + \mu_s\Delta t\left\|\left[\frac{\partial \mathbf{E}}{\partial t}\right]^k\right\|^2_{\Omega_s}. \end{aligned} \tag{20}$$

Straightforward computations show for the third term in (13):

$$\begin{aligned} \int_{\Omega_f} \rho_f J_{k-1}\left[\frac{\partial \mathbf{v}}{\partial t}\right]^k \boldsymbol{\psi}\,\mathrm{d}\mathbf{x} &= \int_{\Omega_f} \frac{\rho_f}{2}\frac{J_k|\mathbf{v}^k|^2 - J_{k-1}|\mathbf{v}^{k-1}|^2}{\Delta t}\,\mathrm{d}\mathbf{x} \\ &\quad - \int_{\Omega_f} \frac{\rho_f|\mathbf{v}^k|^2}{2}\left[\frac{\partial J}{\partial t}\right]^k\mathrm{d}\mathbf{x} + \int_{\Omega_f}\frac{\Delta t\,\rho_f J_{k-1}}{2}\left|\left[\frac{\partial \mathbf{v}}{\partial t}\right]^k\right|^2\mathrm{d}\mathbf{x}. \end{aligned} \tag{21}$$

Applying integration by parts to the fourth (inertia) term in (13) gives

$$\begin{aligned} &\int_{\Omega_f} \rho_f J_k(\nabla\mathbf{v}^k)\mathbf{F}_k^{-1}\left(\mathbf{v}^k - \left[\frac{\partial \mathbf{u}}{\partial t}\right]^k\right)\boldsymbol{\psi}\,\mathrm{d}\mathbf{x} \\ &= -\int_{\Omega_f}\frac{\rho_f}{2}\mathrm{div}\left(J_k\mathbf{F}_k^{-1}\left(\mathbf{v}^k - \left[\frac{\partial \mathbf{u}}{\partial t}\right]^k\right)\right)|\mathbf{v}^k|^2\,\mathrm{d}\mathbf{x} \\ &\quad + \int_{\Gamma_{\mathrm{out}}}\frac{\rho_f}{2}\mathbf{v}^k\cdot\mathbf{n}|\mathbf{v}^k|^2\,\mathrm{d}\mathbf{s}. \end{aligned} \tag{22}$$

Here we used boundary and interface conditions. The fifth term in (13) gives

$$\int_{\Omega_f} 2\mu_f J_k\mathbf{D}_k\mathbf{v}^k : \mathbf{D}_k\boldsymbol{\psi}\,\mathrm{d}\mathbf{x} = \int_{\Omega_f} 2\mu_f J_k\left|\mathbf{D}_k\mathbf{v}^k\right|^2_F\mathrm{d}\mathbf{x},$$

and the next pressure term vanishes due to the incompressibility condition (15). Finally, the last term cancels with similar terms with opposite sign which appear in (21) and (22). Substituting all equalities back into (13), we obtain after some cancellations the following energy balance for the finite element FSI problem with the first order discretization in time:

$$\begin{aligned} &\frac{1}{2\Delta t}\left(\|\rho_s^{\frac12}\mathbf{v}^k\|^2_{\Omega_s} - \|\rho_s^{\frac12}\mathbf{v}^{k-1}\|^2_{\Omega_s}\right) + \frac{\rho_f}{2|\Delta t|}\int_{\Omega_f}\left(J_k|\mathbf{v}^k|^2 - J_{k-1}|\mathbf{v}^{k-1}|^2\right)\mathrm{d}\mathbf{x}\Big\}\text{variation of kinetic energy} \\ &\quad + \frac{\lambda_s}{2\Delta t}\left(\|\mathrm{tr}(\mathbf{E}_k)\|^2_{\Omega_s} - \|\mathrm{tr}(\mathbf{E}_{k-1})\|^2_{\Omega_s}\right) + \frac{\mu_s}{\Delta t}\left(\|\mathbf{E}_k\|^2_{\Omega_s} - \|\mathbf{E}_{k-1}\|^2_{\Omega_s}\right)\Big\}\text{variation of potential energy} \\ &\quad + 2\mu_f\int_{\Omega_f} J_k\left|\mathbf{D}_k(\mathbf{v}^k)\right|^2_F\mathrm{d}\mathbf{x}\Big\}\text{energy dissipation in fluid} \\ &\quad + \frac{\lambda_s\Delta t}{2}\left\|\left[\frac{\partial \mathrm{tr}(\mathbf{E})}{\partial t}\right]^k\right\|^2_{\Omega_s} + \mu_s\Delta t\left\|\left[\frac{\partial \mathbf{E}}{\partial t}\right]^k\right\|^2_{\Omega_s} \\ &\quad + \frac{\rho_f(\Delta t)}{2}\int_{\Omega_f} J_{k-1}\left|\left[\frac{\partial \mathbf{v}}{\partial t}\right]^k\right|^2\mathrm{d}\mathbf{x} + \frac{|\Delta t|}{2}\left\|\rho_s^{\frac12}\left[\frac{\partial \mathbf{v}}{\partial t}\right]^k\right\|^2_{\Omega_s}\Big\}\begin{array}{l}O(\Delta t)\text{dissipative} \\ \text{terms}\end{array} \\ &= -\frac{\rho_f}{2}\int_{\Gamma_{\mathrm{out}}}\{(\mathbf{v}^k\cdot\mathbf{n})_+ + (1-\kappa)(\mathbf{v}^k\cdot\mathbf{n})_-\}|\mathbf{v}^k|^2\,\mathrm{d}\mathbf{s}.\Big\}\begin{array}{l}\text{energy flux through} \\ \text{open boundary}\end{array} \end{aligned}$$

One notes that the above equality resembles the energy balance (12) of the original FSI problem up to several $O(\Delta t)$ terms. In the structure these extra terms are always dissipative. For the fluid we need the following assumption on the ALE displacement field. *Assume that the extension of displacements to the fluid domain is such that for all k it holds $J_k > 0$ in Ω_f*, i.e. the displacements do not tangle the mesh. For the sake of notation simplicity we shall also use $\|\cdot\|_{\Omega_f^k} := \left(\int_{\Omega_f} J_k|\cdot|^2\,\mathrm{d}\mathbf{x}\right)^{\frac12}$, which defines a k-dependent norm for $J_k > 0$. The terms in the fourth group on the left-hand side are non-negative and dropping them changes the equality to inequality. If $\kappa = 1$, then the outflow term is non-negative and standing with

minus sign it can be also dropped. We end up with the inequality:

$$\frac{1}{2}\left\|\rho_s^{\frac{1}{2}}\left[\frac{\partial \mathbf{u}}{\partial t}\right]^k\right\|_{\Omega_s}^2+\frac{\rho_f}{2}\|\mathbf{v}^k\|_{\Omega_f^k}^2 +\frac{\lambda_s}{2}\|\mathrm{tr}(\mathbf{E}_k)\|_{\Omega_s}^2+\mu_s\|\mathbf{E}_k\|_{\Omega_s}^2+2\mu_f(\Delta t)\|\mathbf{D}_k\mathbf{v}^k\|_{\Omega_f^k}^2 \le \frac{1}{2}\left\|\rho_s^{\frac{1}{2}}\left[\frac{\partial \mathbf{u}}{\partial t}\right]^{k-1}\right\|_{\Omega_s}^2+\frac{\rho_f}{2}\|\mathbf{v}^{k-1}\|_{\Omega_f^{k-1}}^2+\frac{\lambda_s}{2}\|\mathrm{tr}(\mathbf{E}_{k-1})\|_{\Omega_s}^2 +\mu_s\|\mathbf{E}_{k-1}\|_{\Omega_s}^2.$$

The energy estimate follows if we sum up the above inequalities for $k=0,\dots,N-1$:

$$\frac{1}{2}\left\|\rho_s^{\frac{1}{2}}\left[\frac{\partial \mathbf{u}}{\partial t}\right]^N\right\|_{\Omega_s}^2+\frac{\lambda_s}{2}\|\mathrm{tr}(\mathbf{E}_N)\|_{\Omega_s}^2+\mu_s\|\mathbf{E}_N\|_{\Omega_s}^2 +\frac{\rho_f}{2}\|\mathbf{v}^N\|_{\Omega_f^N}^2+2\mu_f\sum_{k=1}^{N}\Delta t\|\mathbf{D}_k\mathbf{v}^k\|_{\Omega_f^k}^2 \le \|\rho_s^{\frac{1}{2}}\mathbf{v}^0\|_{\Omega_s}^2+\frac{\rho_f}{2}\|\mathbf{v}^0\|_{\Omega_f^0}^2+\frac{\lambda_s}{2}\|\mathrm{tr}(\mathbf{E}_0)\|_{\Omega_s}^2+\mu_s\|\mathbf{E}_0\|_{\Omega_s}^2. \quad (23)$$

We summarize the results in the following theorem.

Theorem 1. *Assume that the extension of the finite element displacement field to Ω_f is such that $J_k>0$ for all $k=1,\dots,N-1$, and $\kappa=1$. Then the solution to the finite element method (13)–(16) satisfies the a priori estimate (23).*

5. Numerical experiments

This section assesses the performance of the monolithic FSI FE method on two benchmark problems: the propagation of a pressure impulse in a flexible tube and the interaction of a three-dimensional clamped beam with a fluid flowing in a pipe, the benchmark tests suggested in [21] and [26], respectively. The first test problem is related to the blood flow through a compliant artery, and it has been extensively considered in the literature for validating the performance of FSI solvers, e.g. [14,18,22,23,34,39]. Since the problem is an idealization of a practical setup, no experimental data is available and the test serves to validate mesh convergence and the physical plausibility of the computed solutions. For the clamped beam in a pipe flow problem, experimental measurements are available and documented in [26] with the intention to provide a challenging FSI test case for the rigorous testing of FSI algorithms. This test case utilizes the geometry obtained from computer-aided design, but is also motivated by biomedical applications. Flow and structure statistics were measured for both steady-state and transient laminar flows at maximal Reynolds numbers of 651 and 1283, reflecting Re numbers found for the cardiovascular flows. The benchmark has been recently used to validate numerical FSI solvers in [11,27,35].

For all experiments we use P2-P1 (Taylor–Hood) elements for velocity and pressure variables and P2 elements for displacements. The scheme (13)–(16) is implemented on the basis of the open source package Ani3D [36]. To handle the nonlinear system on each time step, we linearly extrapolate all geometric terms and the advection velocity in the inertia term from two previous time steps. The resulting linear system is solved by the multifrontal sparse direct solver MUMPS [1]. Application of the direct solver is feasible, since in all numerical tests the number of degrees of freedom is moderate (about 10^5 d.o.f.). The latter is achieved thanks to the higher than the second order accuracy of the method combined with 3D mesh adaptation. For finer meshes, one would need to solve the linear systems iteratively. Parallel preconditioning for such FSI systems has been addressed, e.g., in [33].

For the continuous extension of the displacement field $\mathbf{u}$ in (1), we use the following elasticity equation [35] for the velocity of the displacement:

$$-\mathrm{div}\left[J\left(\lambda_m\mathrm{tr}\left(\nabla\left[\frac{\partial \mathbf{u}}{\partial t}\right]^k\mathbf{F}^{-1}\right)\mathbf{I} +\mu_m\left(\nabla\left[\frac{\partial \mathbf{u}}{\partial t}\right]^k\mathbf{F}^{-1}+\left(\nabla\left[\frac{\partial \mathbf{u}}{\partial t}\right]^k\mathbf{F}^{-1}\right)^T\right)\right)\mathbf{F}^{-T}\right] =0 \text{ in } \Omega_f. \quad (24)$$

The boundary condition $\left[\frac{\partial \mathbf{u}}{\partial t}\right]^k=\mathbf{v}^k$ is used on the interface. The space dependent auxiliary parameters were chosen as shown:

$$\mu_m=\mu_s|\Delta_e|^{-1.2},\ \lambda_m=16\mu_m,$$

where $|\Delta_e|$ denotes the physical volume of a mesh tetrahedron Δ_e subjected to displacement from the previous time step.

5.1. Pressure wave in flexible tube

The problem configuration consists of an incompressible viscous flow through an elastic tube with circular cross-section. The tube is 50mm long, it has inner diameter of 10mm and the wall is 1mm thick. The fluid density is 10^{-3}g/mm^3 and kinematic viscosity is 3mm^2/s. The wall has density $\rho_s=1.2\cdot10^{-3}$g/mm^3. The Saint Venant–Kirchhof hyperelastic model is used with elastic modulus $E=3\cdot10^5$g/mm/s^2 and Poisson's ratio $\nu=0.3$. Initially the fluid is at rest and the tube is non-deformed. The tube is fixed at both ends. On the left open boundary of the tube, the external pressure p_{ext} is set to $1.333\cdot10^3$Pa for $t\in(0,3\cdot10^{-3})$s and zero afterwards, while on the right open boundary the external pressure p_{ext} is zero throughout the experiment. This generates a pressure impulse that travels along the tube. The external pressure is incorporated into (13)–(16) through the open boundary condition $\boldsymbol{\sigma}_f\mathbf{F}^{-T}\mathbf{n}=p_{ext}\mathbf{n}$.

We built three computational meshes (coarse, fine and finer) for this experiment. On each level of refinement the mesh size was decreased by approximately a factor of $\sqrt{2}$. The resulting numbers of tetrahedra in the fluid and solid subdomains, respectively, are 13,200 and 6336 for coarse, 29,202 and 11,904 for fine, and 89,232 and 38,016 for finer. We set $\Delta t=10^{-4}$s. For this problem, we do not use outflow boundary stabilization, i.e. $\kappa=0$ on both open boundaries.

Fig. 2 depicts the computed velocity field in the middle cross-section and wall displacement exaggerated by a factor of 10 for clarity. The results are similar to those found in other publications cited. Fig. 3 shows the time variations of the radial and axial components of the displacement of the inner tube wall at half the length of the pipe. Both graphs suggest that the finer mesh results are close to convergence. The maximum relative deviation between coarse and fine mesh displacement 2.1% in the axial component and 2.7% in the radial component, which decreases to maximum relative deviation between fine and finer mesh to 0.7% in the axial component and 2.3% in the radial component. Both plots are consistent with the results reported in [18].

Finally, we demonstrate stability bound (23) for this particular problem. Since the problem setup involves specification of non-zero pressure on the inflow for the first 30 time steps, for checking (23) we consider the computed velocity at $t=0.003$s as the initial condition, and evaluate all quantities in (23) for $t\in[0.003s,0.02s]$. For the right-hand side of (23), the computed value was 1197.7 μJ, while for the left-hand side it was 247.62 μJ.

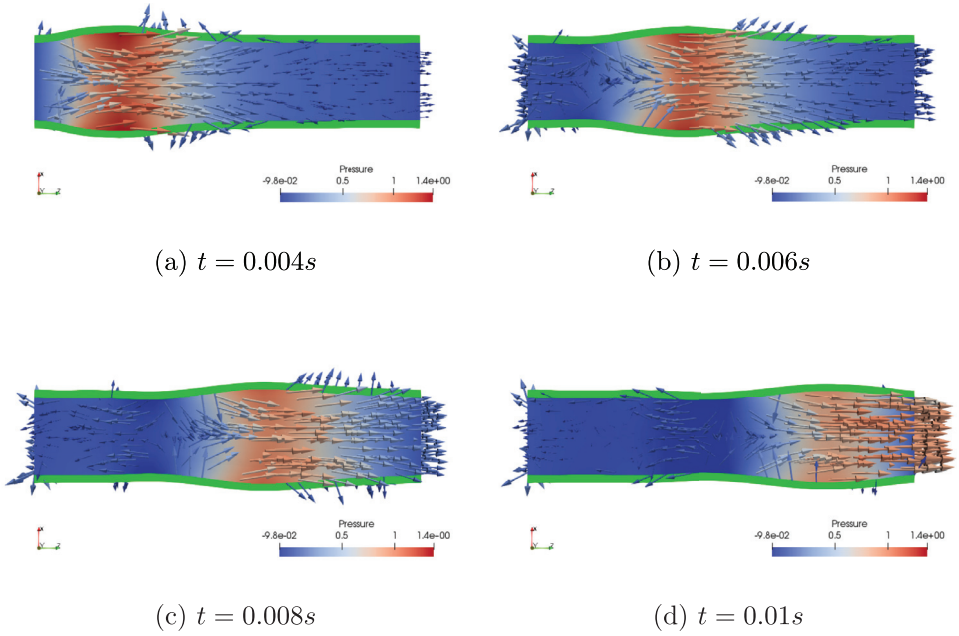

(a) $t = 0.004s$ (b) $t = 0.006s$

(c) $t = 0.008s$ (d) $t = 0.01s$

Fig. 2. Pressure wave: middle cross-section velocity field, pressure distribution, velocity vectors and 10-fold enlarged structure displacement for several time instances.

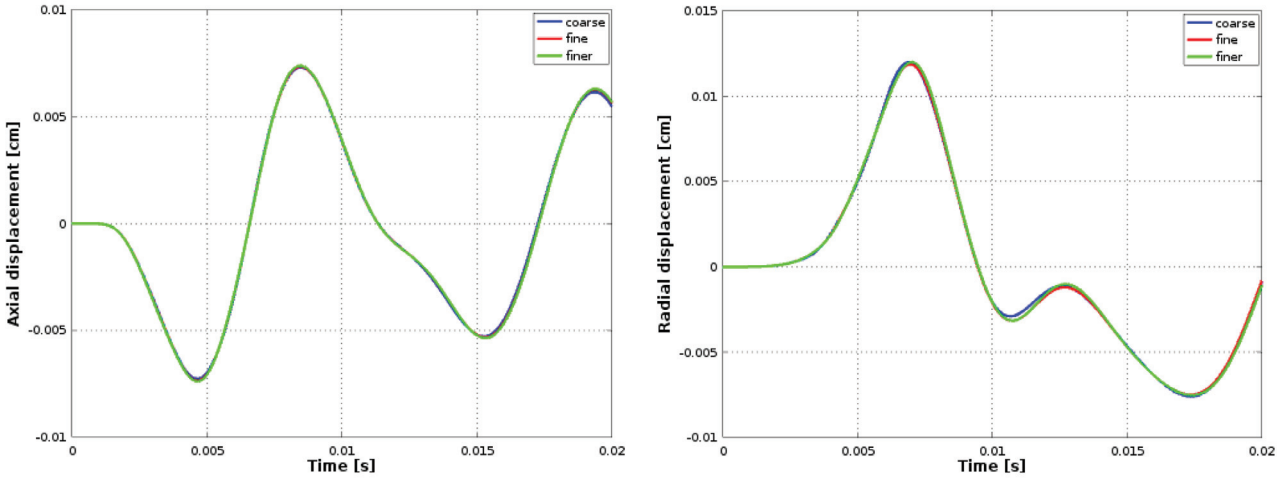

(a) axial component (b) radial component

Fig. 3. Pressure wave: The axial and radial components of displacement of the inner tube wall at half the length of the pipe. Solutions are shown for three mesh sequentially refined meshes (see the text). The plots are almost indistinguishable.

5.2. Clamped beam in a pipe flow

The flow chamber is a cylindrical domain aligned with z-axis with length 173.55mm, and diameter 76.2mm, see Fig. 4. Two inlet pipes of diameter 21.9mm and length 29.5mm merge smoothly into a single outlet. The inlet cross-sections are circles with centers at (0,27.15,-29.5) and (0,-27.15,-29.5). A silicon filament is attached to the wall in the merging section $z = 0$. The filament (solid body) has dimensions $2 \times 11 \times 65$mm. According to [26], the density of the silicone filament is $\rho_s = 1063\text{kg/m}^3$. Uniaxial traction data from [26] yield the Young modulus $E = 2.1626\,10^5$Pa and Poisson ratio $\nu = 0.3151$ [35]. The gravity force 9.81m/s^2 acts along the y-direction. For Phase I and Phase II of the experiment, the fluid density is 1163.3kg/m^3 and 1164kg/m^3, respectively, and the kinematic viscosity is $10.75\text{mm}^2/\text{s}$ and $11.49\text{mm}^2/\text{s}$, respectively.

For Phase I experiment, the parabolic flow profiles are prescribed on both inflow boundaries with a smooth increase of the peak velocity values (z-component) from 0 to 615mm/s in the top section and 630mm/s in the bottom one and further stay constant. For Phase II, the inflow condition is periodic with the frequency $1/6\text{s}^{-1}$. The inflow velocity profiles are parabolic in each component with peak velocities recovered from the experimental data. These measured peak inflow velocities are shown in Fig. 5. There is a difference between y-velocity components profiles at top and bottom cross-sections; following [26] we set $v_y = 0$ at the inflow of the bottom pipe.

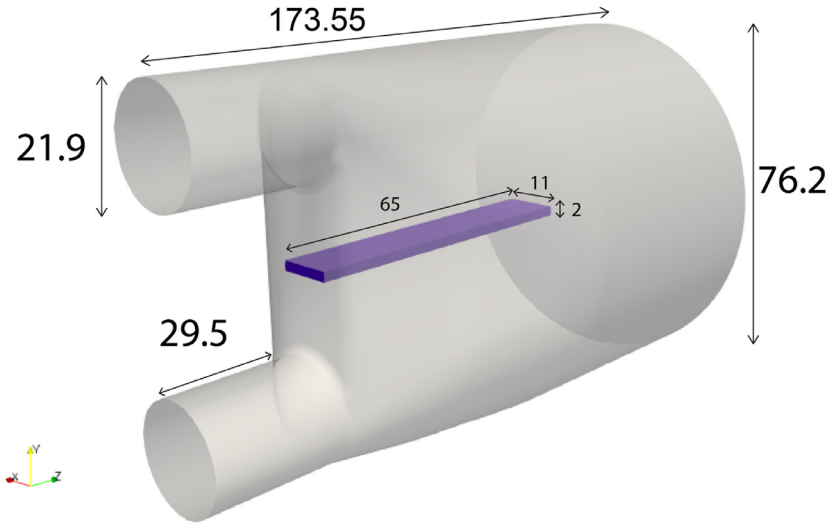

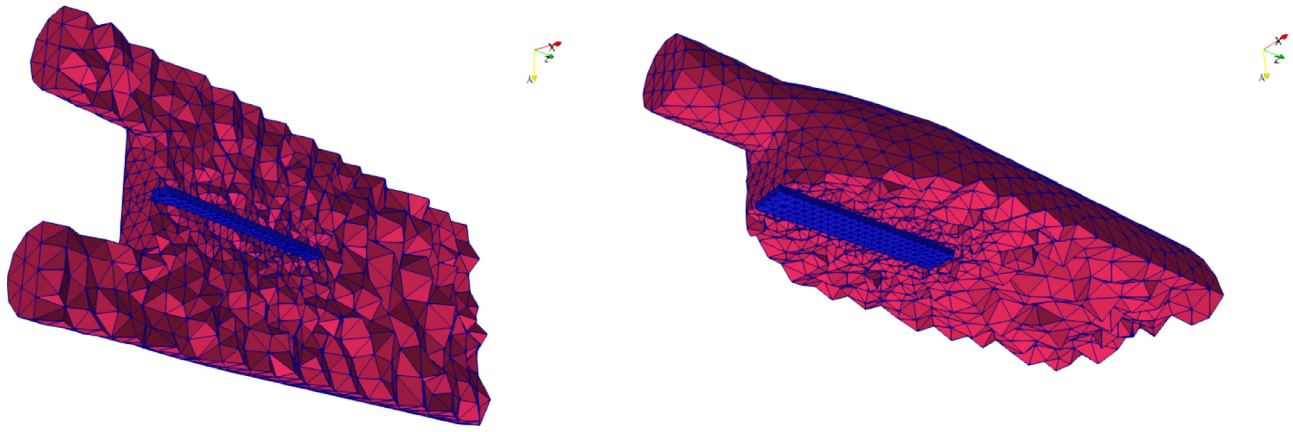

Fig. 4. FSI benchmark domain (top); Computational mesh for fluid and structure domains (bottom).

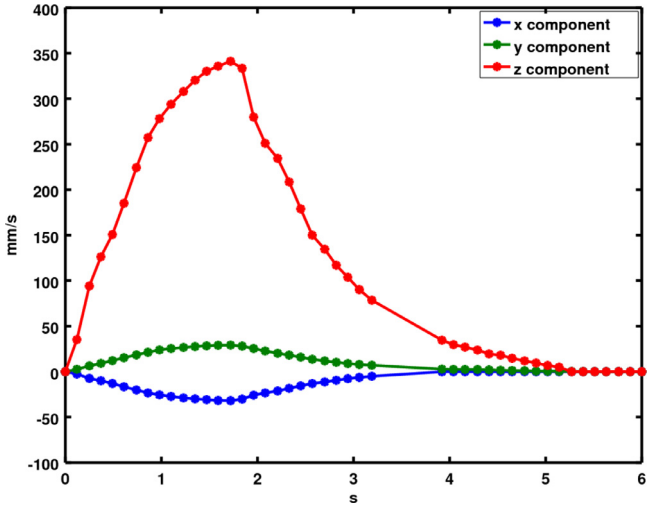

Fig. 5. Measured peak velocity for parabolic inflow used for the boundary condition in the computations (Phase II).

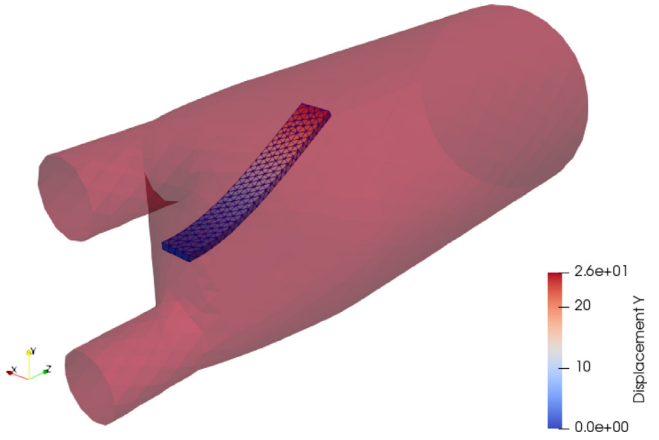

Fig. 6. An equilibrium position of the elastic beam in the hydrostatic equilibrium.

The computational mesh is built for the stress-free configuration, cf. Fig. 4. The tetrahedral mesh is fitted to the fluid–solid boundary and uses two layers of tetrahedra to resolve the silicon filament. The fluid domain is tesselated into 28,712 tetrahedra, and the number of tetrahedra in the solid domain is 733. For P2-P2-P1 elements (displacement–velocity–pressure) this results in the total number of 254,439 unknowns.

On the outflow boundary we prescribe directional outflow condition as in (6) with $\kappa = 1$ and $\mathbf{g}_N = g y \mathbf{n}$, where g is the acceleration of gravity.

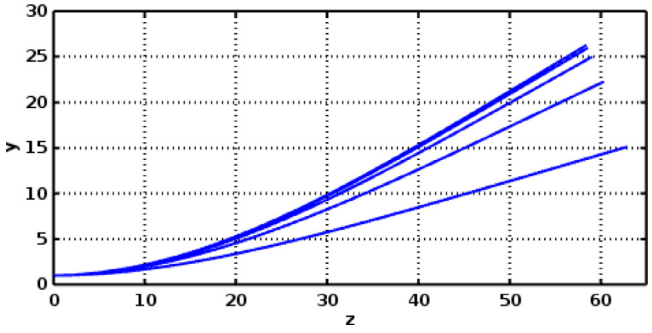

Fig. 7. Evolution of the beam from the neutral position to the hydrostatic equilibrium. Position of the middle line for the beam is shown at times $t = 1.65 \cdot k$ sec, $k = 1, \ldots, 5$.

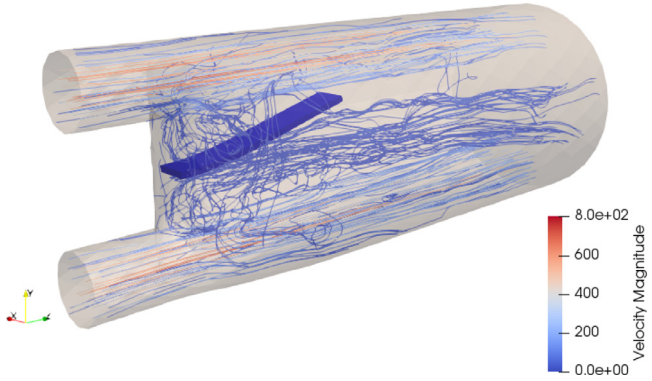

Fig. 8. Visualization of the flow in Phase I. The figure shows streamlines colored by the velocity magnitude (mm/s).

5.3. Hydrostatic equilibrium

We first compute the hydrostatic equilibrium solution under the action of the gravity force. The fluid density and viscosity were taken the same as for Phase I. To avoid unnecessary fluctuations and accelerate convergence to equilibrium, we added a damping term for the solid in the form of the friction force $-\alpha \mathbf{v}$, where $\alpha = 10^{-4}$kg/mm^3/s. The final position of the filament and snapshots of its position in different time moments are illustrated in Figs. 6, 7 respectively. We further use this equilibrium solution as the initial condition in Phases I and II.

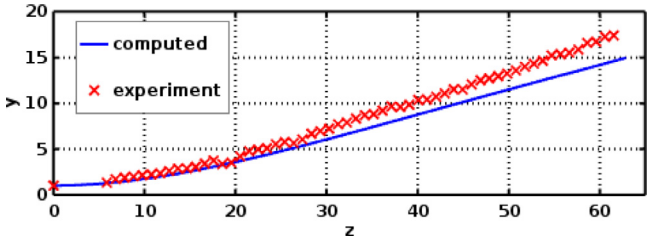

Fig. 9. Displacement of the beam middle line on its upper surface in Phase I.

5.4. Phase I

We run calculations up to $T = 23.5$ s with time step $\Delta t = 10^{-2}$ s. After a short transition phase, the solution attains an equilibrium, which can be slightly perturbed by flow dynamics. Fig. 8 illustrates the final position of the deformed elastic beam and a passing flow. We note the formation of recirculation zone behind the $z = 0$ wall where the filament is attached.

Fig. 9 compares the computed displacement of the silicon beam to the data recorded in the experiment. We see that the numerical results underestimate the experimental data, although the overall agreement is good and the discrepancy is comparable to the deviation between numerical and experimental results found in references [27,35]. In [11] the authors reported the perfect matching of experimental and numerical results, which we are unable to achieve. The discrepancy in results might be caused by the existence of multiple steady states for this problem or by the treatment of outflow boundary, which is set not sufficiently far from the beam. We next compare in Fig. 10 the computed fluid velocity y and z components at cross-sections $z = 10$ and $z = 30$ with those acquired by MRI techniques and re-

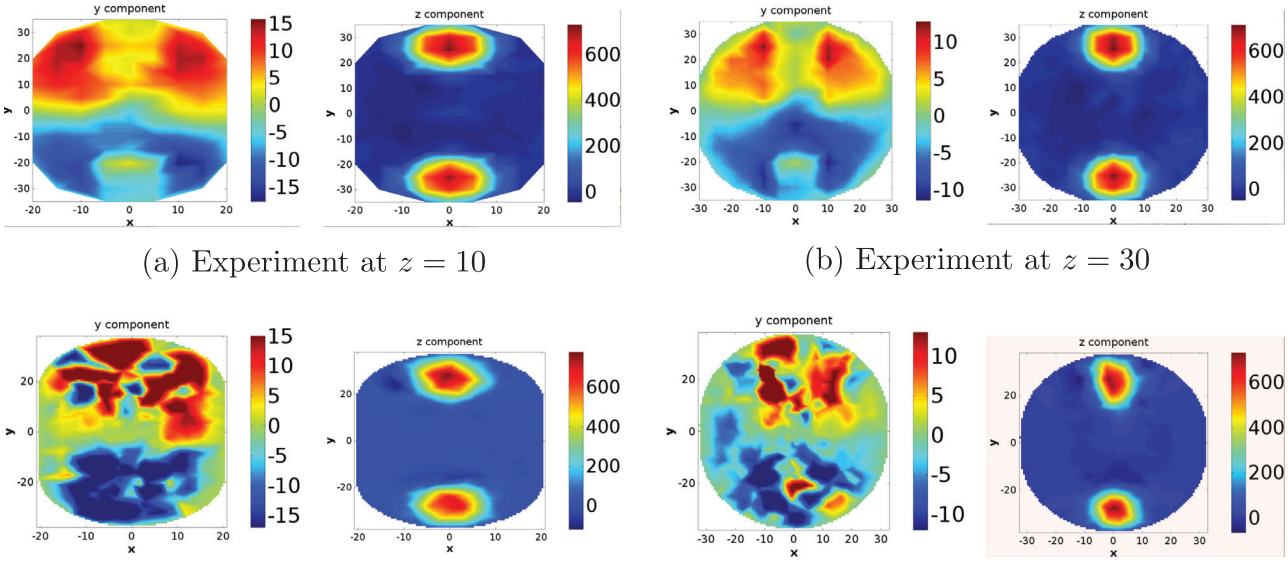

Fig. 10. Fluid velocity components in Phase I. Comparison of the experimental data and the numerical solution at the cross-sections $z = 10$ and $z = 30$.

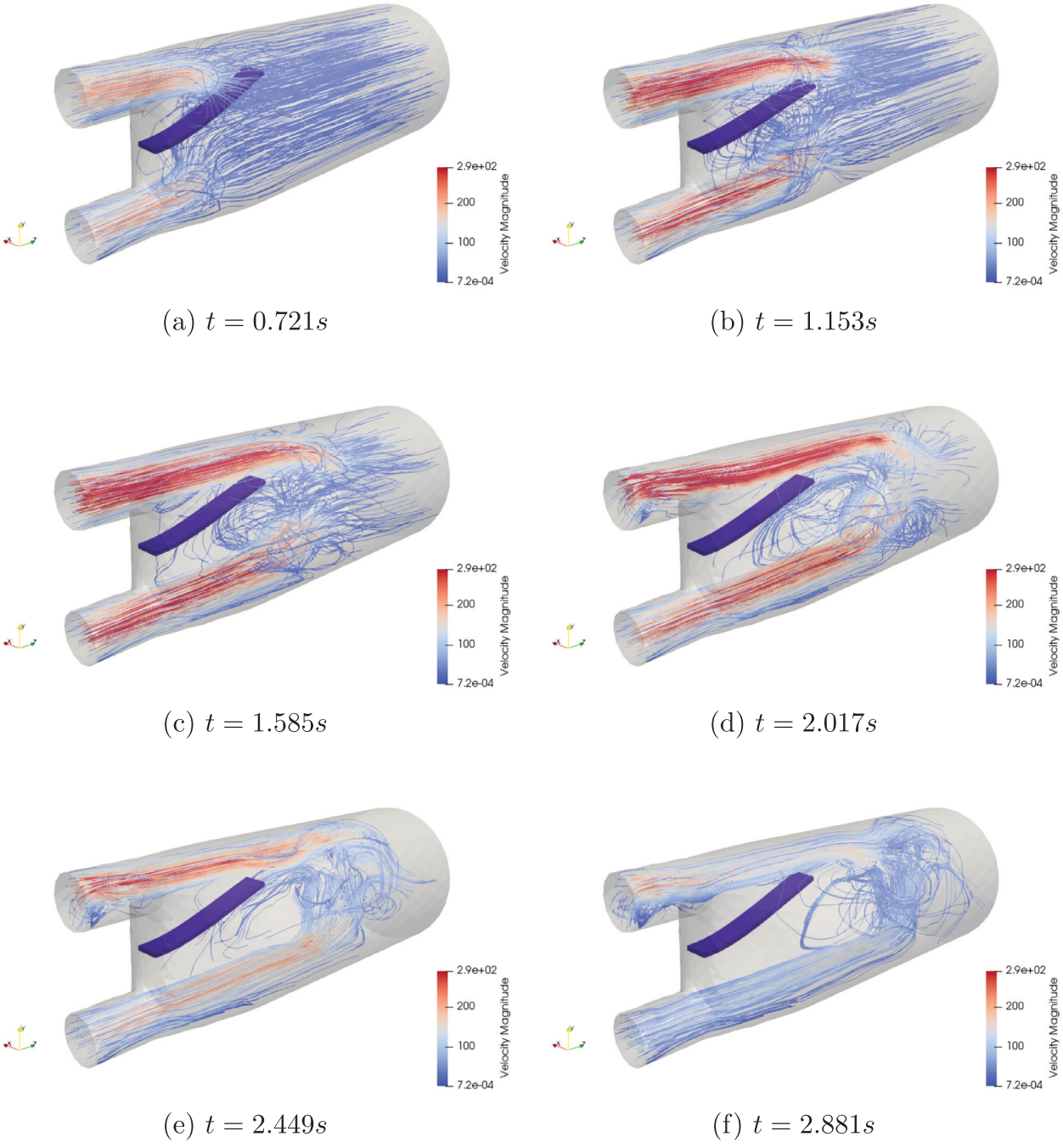

Fig. 11. Snapshots of the flow at Phase II. The figure shows streamlines colored by the velocity magnitude (mm/s).

ported in [26]. Some mismatch of numerical and experimental beam positions seem to produce the discrepancy in y-component of numerical and experimental fluid velocities. At the same time, z-component demonstrates good agreement with experimental data.

The MUMPS algebraic solver was executed with 8 MPI processes, using 10 CPU cores for each process for parallel BLAS operations. The entire computation in Phase I took 14.7 hours in total (12.7 hours spent for linear solvers and 1.93 hours for matrix and right-hand side assembly). One time step took 22.5 seconds in average to complete.

5.5. Phase II

In this experiment, a pulsatile inflow results in the periodic solution. We run calculations for two periods, up to $T = 12$ s with time step $\Delta t = 10^{-2}$ s. Below we use the computed data for the first period to ease the comparison with [11,27,35], where only the first period results are shown.

Fig. 11 illustrates the predicted flow in Phase II. We note some unsteady vortical structures passing the beam and forming in the wake. These structures interact with the filament and may influence its motion.

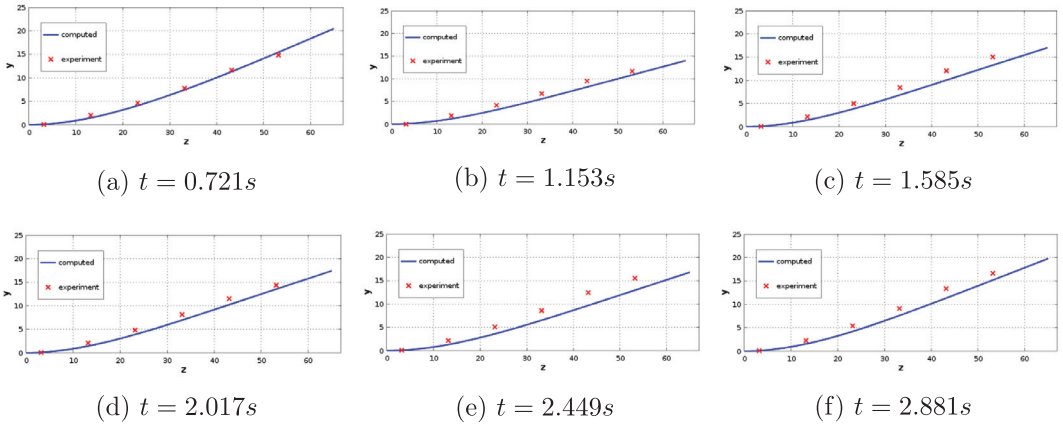

Fig. 12. Phase II: Computed and experimentally recorded y-displacement of the beam centerline at $x = 0$ for several time instances.

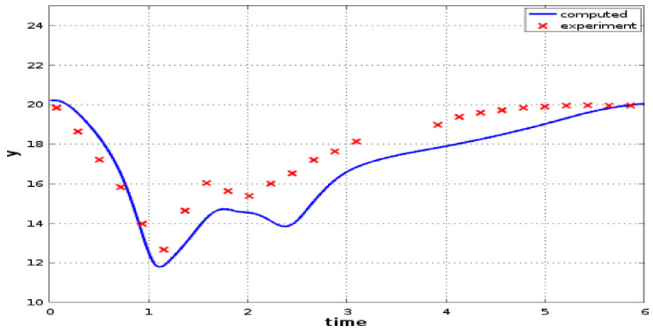

Fig. 13. Phase II: Track of the computed y-displacement of the point in the structure with coordinate $z \approx 53$, $x = 0$ for $t \in [0, 6]$ and recorded experimental data.

Figs. 12 and 13 present the comparison of the recorded and predicted displacements of the silicon beam over one period. The experimental data is only provided for 6 positions as shown in Fig. 12. The numerical method is able to perfectly predict the maximum deflection of the beam. The dynamics of the beam in this experiment with unsteady flow is driven by the competition between normal stresses exerted on the beam by upcoming flow jet and the buoyancy force. The basic features of the beam motion including the swing and time when the beam has minimal and maximal deflections are well captured by the numerical method, see Fig. 13.

Fig. 14 compares experimental measurements and predicted results of the fluid velocity components at different time steps for cross-section $z = 33.5$. This is the most remote from the inlet cross-section with recorded data for three velocity components and so the hardest for numerical prediction. The velocity z-component is somewhat underresolved, suggesting that the computed solution is slightly diffusive. However the main patterns of the flow are well captured.

Similarly to Phase I, we used 8 MPI processes for the MUMPS solver, but with 12 CPU cores per each process. This resulted in 6 hours of the overall computation (5.2 hours spent for linear solvers and 0.8 hours for matrix and right-hand side assembly), with 18.1 seconds per time step.

6. Conclusions

In the paper we addressed stability and performance of a monolithic finite element method for incompressible fluid – hyperelastic structure interaction problems. We demonstrated that the method of lines for the ALE/Lagrangian formulation of fluid/structure equations in a reference domain is a feasible ap-

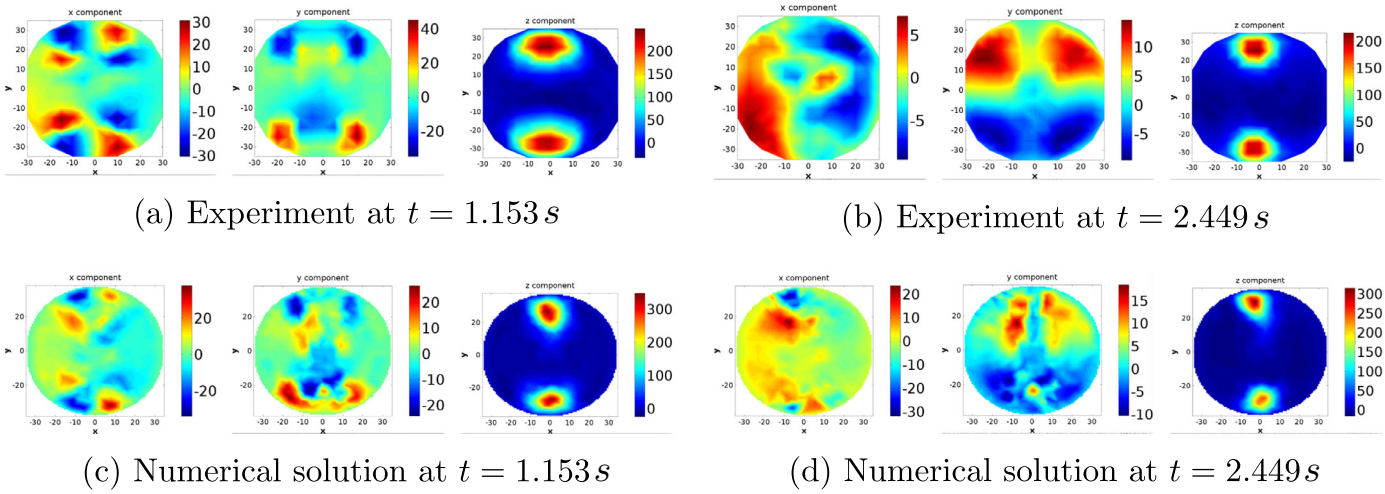

Fig. 14. Fluid velocity components in Phase II. Comparison of the experimental data and the numerical solution on the cross-section $z = 33.5$.

proach, and time-dependent coefficients can be time-lagged without undermining stability. In fact, numerical experiments demonstrated that in practice the size of time step is dictated by accuracy consideration rather than any stability condition. The computed kinetic, potential energy and energy dissipation were found to satisfy the theoretically predicted bound. Although the method is completely formulated in the reference triangulated domain, it was found to share limitations with those FE ALE formulations that update mesh in a physical domain. Namely, finding a suitable extension of the displacement field to the fluid domain is crucial for the stability of computations and becomes an increasingly challenging task when structural displacements are large. If a suitable prolongation technique is available (in this paper (24) was found to work well), then the presented method is stable and predictive in realistic 3D settings even with a modest overall number of degrees of freedom.

Acknowledgements

We are thankful to Miguel Fernandez and Andreas Hessenthaler for helpful discussions regarding the setup and numerical pitfalls of the clamped beam in a pipe flow benchmark. We also thank Alexander Danilov for generation of the computational meshes.

References

[1] Amestoy PR, Duff IS, L'Excellent J-Y, Koster J. A fully asynchronous multifrontal solver using distributed dynamic scheduling. SIAM J Matrix Anal Appl 2001;23(1):15–41.
[2] Aulisa E, Bna S, Bornia G. A monolithic ALE Newton–Krylov solver with multigrid-Richardson–Schwarz preconditioning for incompressible fluid-structure interaction. Comput Fluid 2018.
[3] Badia S, Nobile F, Vergara C. Fluid–structure partitioned procedures based on Robin transmission conditions. J Comput Phys 2008;227(14):7027–51.
[4] Basting S, Quaini A, Čanić S, Glowinski R. Extended ALE method for fluid–structure interaction problems with large structural displacements. J Comput Phys 2017;331:312–36.
[5] Bazilevs Y, Gohean J, Hughes T, Moser R, Zhang Y. Patient-specific isogeometric fluid–structure interaction analysis of thoracic aortic blood flow due to implantation of the jarvik 2000 left ventricular assist device. Comput Methods Appl Mech Eng 2009;198(45–46):3534–50.
[6] Bazilevs Y, Takizawa K, Tezduyar TE. Computational fluid-structure interaction: methods and applications. Chichester: John Wiley & Sons; 2013.
[7] Bertoglio C, Caiazzo A, Bazilevs Y, Braack M, Esmaily M, Gravemeier V, et al. Benchmark problems for numerical treatment of backflow at open boundaries. Int J Numer Method Biomed Eng 2017.
[8] Bodnár T, Galdi GP, Nečasová Š. Fluid–structure interaction and biomedical applications. Basel: Springer; 2014.
[9] Boffi D, Gastaldi L. A fictitious domain approach with lagrange multiplier for fluid-structure interactions. Numerische Mathematik 2017;135(3):711–32.
[10] Braack M, Mucha PB, Zajaczkowski WM. Directional do-nothing condition for the Navier-Stokes equations. J Comput Math 2014;32(5):507–21.
[11] Chiang C-Y, Pironneau O, Sheu TW, Thiriet M. Numerical study of a 3D Eulerian monolithic formulation for incompressible fluid-structures systems. Fluids 2017;2(2):34.
[12] Degroote J, Bruggeman P, Haelterman R, Vierendeels J. Stability of a coupling technique for partitioned solvers in FSI applications. Comput Struct 2008;86(23):2224–34.
[13] Degroote J, Haelterman R, Annerel S, Bruggeman P, Vierendeels J. Performance of partitioned procedures in fluid-structure interaction. Comput Struct 2010;88(7):446–57.
[14] Degroote J, Haelterman R, Annerel S, Bruggeman P, Vierendeels J. Performance of partitioned procedures in fluid–structure interaction. Comput Struct 2010;88(7–8):446–57.
[15] Donea J, Giuliani S, Halleux JP. An arbitrary Lagrangian-Eulerian finite element method for transient dynamic fluid-structure interactions. Comput Methods Appl Mech Eng 1982;33(1):689–723.
[16] Dowell EH, Hall KC. Modeling of fluid-structure interaction. Annu Rev Fluid Mech 2001;33(1):445–90.
[17] Dunne T, Rannacher R. Adaptive finite element approximation of fluid-structure interaction based on an eulerian variational formulation. In: Fluid-structure interaction. Springer; 2006. p. 110–45.
[18] Eken A, Sahin M. A parallel monolithic algorithm for the numerical simulation of large-scale fluid structure interaction problems. Int J Numer Methods Fluids 2016;80(12):687–714.
[19] Fernández MA, Gerbeau J-F, Grandmont CA. A projection semi-implicit scheme for the coupling of an elastic structure with an incompressible fluid. Int J Numer Methods Eng 2007;69(4):794–821.
[20] Formaggia L, Quarteroni A, Veneziani A. Cardiovascular mathematics: modeling and simulation of the circulatory system, 1. Milan: Springer Science & Business Media; 2010.
[21] Formaggia L, Gerbeau J-F, Nobile F, Quarteroni A. On the coupling of 3D and 1d Navier–Stokes equations for flow problems in compliant vessels. Comput Methods Appl Mech Eng 2001;191(6–7):561–82.
[22] Gee MW, Küttler U, Wall WA. Truly monolithic algebraic multigrid for fluid–structure interaction. Int J Numer Methods Eng 2011;85(8):987–1016.
[23] Gerbeau J-F, Vidrascu M. A quasi-Newton algorithm based on a reduced model for fluid-structure interaction problems in blood flows. ESAIM Math Model Numer Anal 2003;37(4):631–47.
[24] Grandmont C, Guimet V, Maday Y. Numerical analysis of some decoupling techniques for the approximation of the unsteady fluid structure interaction. Math Models Methods Appl Sci 2001;11(08):1349–77.
[25] Heil M, Hazel AL, Boyle J. Solvers for large-displacement fluid-structure interaction problems: segregated versus monolithic approaches. Comput Mech 2008;43(1):91101.
[26] Hessenthaler A, Gaddum N, Holub O, Sinkus R, Röhrle O, Nordsletten D. Experiment for validation of fluid-structure interaction models and algorithms. Int J Numer Method Biomed Eng 2017;33(9).
[27] Hessenthaler A, Röhrle O, Nordsletten D. Validation of a non-conforming monolithic fluid-structure interaction method using phase-contrast mri. Int J Numer Method Biomed Eng 2017;33(8).
[28] Hirt CW, Amsden AA, Cook JL. An arbitrary Lagrangian-Eulerian computing method for all flow speeds. J Comput Phys 1974;14(3):227–53.
[29] Hou G, Wang J, Layton A. Numerical methods for fluid-structure interaction – a review. Commun Comput Phys 2012;12(2):337–77.
[30] Hron J, Turek S. A monolithic FEM/multigrid solver for an ALE formulation of fluid-structure interaction with applications in biomechanics. Springer Berlin Heidelberg; 2006.
[31] Hubner B, Walhorn E, Dinkler D. A monolithic approach to fluid-structure interaction using space-time finite elements. Comput Methods Appl Mech Eng 2004;193(23):2087–104.
[32] Hughes TJR, Liu WK, Zimmermann TK. Lagrangian-Eulerian finite element formulation for incompressible viscous flows. Comput Methods Appl Mech Eng 1981;29(3):329–49.
[33] Kong F, Cai X-C. A scalable nonlinear fluid structure interaction solver based on a Schwarz preconditioner with isogeometric unstructured coarse spaces in 3D. J Comput Phys 2017;340:498–518.
[34] Küttler U, Wall WA. Fixed-point fluid–structure interaction solvers with dynamic relaxation. Comput Mech 2008;43(1):61–72.
[35] Landajuela M, Vidrascu M, Chapelle D, Fernández MA. Coupling schemes for the FSI forward prediction challenge: comparative study and validation. Int J Numer Method Biomed Eng 2017;33(4).
[36] Lipnikov K, Vassilevski Y, Danilov A, et al. Advanced Numerical Instruments 3D. http://sourceforge.net/projects/ani3d.
[37] Lozovskiy A, Olshanskii MA, Salamatova V, Vassilevski YV. An unconditionally stable semi-implicit FSI finite element method. Comput Methods Appl Mech Eng 2015;297:437–54.
[38] Lozovskiy A, Olshanskii MA, Vassilevski YV. A quasi-Lagrangian finite element method for the Navier-Stokes equations in a time-dependent domain. Comput Methods Appl Mech Engrg 2018;333:55–73.
[39] Malan A, Oxtoby OF. An accelerated, fully-coupled, parallel 3D hybrid finite-volume fluid–structure interaction scheme. Comput Methods Appl Mech Eng 2013;253:426–38.
[40] Michler C, Hulshoff SJ, van Brummelen EH, de Borst R. A monolithic approach to fluid-structure interaction. Comput Fluid 2004;33(5):839–48.
[41] Mok D, Wall W. Partitioned analysis schemes for the transient interaction of incompressible flows and nonlinear flexible structures. Trend Comput Struct Mech Barc 2001.
[42] Muddle RL, Mihajlović M, Heil M. An efficient preconditioner for monolithically-coupled large-displacement fluid–structure interaction problems with pseudo-solid mesh updates. J Comput Phys 2012;231(21):7315–34.
[43] Nobile F. Numerical approximation of fluid-structure interaction problems wlth application to haemodynamics. Politecnico di Milano; 2001. Ph.D. thesis.
[44] Nobile F, Pozzoli M, Vergara C. Inexact accurate partitioned algorithms for fluid–structure interaction problems with finite elasticity in haemodynamics. J Comput Phys 2014;273:598–617.
[45] Ryzhakov PB, Rossi R, Idelsohn SR, Onate E. A monolithic Lagrangian approach for fluid-structure interaction problems. Comput Mech 2010;46(6):883–99.
[46] Ryzhakov P, Marti J, Idelsohn S, Oñate E. Fast fluid–structure interaction simulations using a displacement-based finite element model equipped with an explicit streamline integration prediction. Comput Methods Appl Mech Eng 2017;315:1080–97.
[47] Swim E, Seshaiyer P. A nonconforming finite element method for fluid–structure interaction problems. Comput Methods Appl Mech Eng 2006;195(17):2088–99.
[48] Temam R. Navier-stokes equations: Theory and numerical analysis, 343. AMS Chelsea Publishing; 2001. 408 pp; ISBN: 978-0-8218-2737-6.
[49] Tezduyar TE, Sathe S, Cragin T, Nanna B, Conklin B, Pausewang J, et al. Modelling of fluid–structure interactions with the space–time finite elements: arterial fluid mechanics. Int J Numer Methods Fluids 2007;54(6–8):901–22.
[50] Tezduyar TE, Sathe S, Stein K. Solution techniques for the fully discretized equations in computation of fluid–structure interactions with the space–time formulations. Comput Methods Appl Mech Eng 2006;195(41):5743–53.

[51] Tu J, Inthavong K, Wong KKL. Computational hemodynamics–theory, modelling and applications. Netherlands: Springer; 2015. doi:10.1007/978-94-017-9594-4.
[52] Van Brummelen E. Partitioned iterative solution methods for fluid–structure interaction. Int J Numer Methods Fluids 2011;65(1–3):3–27.
[53] Wick T. Fluid-structure interactions using different mesh motion techniques. Comput Struct 2011;89(13–14):1456–67.
[54] Yu Y, Kamensky D, Hsu M-C, Lu XY, Bazilevs Y, Hughes TJ. Error estimates for dynamic augmented Lagrangian boundary condition enforcement, with application to immersogeometric fluid–structure interaction. Math Models Methods Appl Sci 2017.
[55] Zhu M, Scott MH. Unified fractional step method for Lagrangian analysis of quasi-incompressible fluid and nonlinear structure interaction using the PFEM. Int J Numer Methods Eng 2017;109(9):1219–36.